

## Dynamic Forces between a Moving Particle and a Deformable Drop

Grant B. Webber,<sup>\*,†,‡</sup> Rogério Manica,<sup>†,§,#</sup> Scott A. Edwards,<sup>†,§</sup> Steven L. Carnie,<sup>†,§</sup>  
Geoffrey W. Stevens,<sup>†,‡</sup> Franz Grieser,<sup>†,||</sup> Raymond R. Dagastine,<sup>\*,†,‡</sup> and Derek Y.C. Chan<sup>§,⊥,#</sup>

Particulate Fluids Processing Centre, Department of Chemical and Biomolecular Engineering, Department of Mathematics and Statistics, and School of Chemistry, The University of Melbourne, Victoria, 3010, Australia, Department of Mathematics, National University of Singapore, Singapore 117543, Institute of High Performance Computing, Singapore 117543

Received: August 3, 2007; In Final Form: October 9, 2007

The dynamic interaction forces between a solid silica particle and an immobilized tetradecane droplet have been measured using atomic force microscopy. The dominant colloidal forces are repulsive electrical double layer interactions due to the partitioning of added sodium dodecyl sulfate to the deformable oil/water (O/W) interface. Over a range of drive velocities up to 50  $\mu\text{m/s}$ , these colloidal forces, plus hydrodynamic interactions due to fluid flow in the aqueous film ( $\sim 22$  nm thick) between the particle and O/W interface, as well as deformations of the interface, contribute to the overall dynamic force between the silica particle (radius  $\sim 12$   $\mu\text{m}$ ) and tetradecane drop (radius of curvature  $\sim 55$   $\mu\text{m}$ ). Within the tolerance of experimental parameters, excellent agreement is observed between the measured forces and those predicted by a theory that accounts for the above phenomena. The theory also furnishes details not directly measurable, such as the time-dependent deformations and velocities of the O/W interface and variations of the thickness of the aqueous film between the particle and the drop during the course of the experiment.

### 1. Introduction

The use of the atomic force microscope (AFM) to measure static interaction forces between two solid surfaces has been well established over recent decades.<sup>1–4</sup> Innovative developments have focused the application of AFM on more complicated measurements, in particular the measurement of dynamic interaction forces and the interrogation of interfacial forces where one or more surface is deformable.<sup>5–11</sup> These forces are of importance in a range of biological processes including cell–cell interactions, chemical formulations such as emulsion formation and stability, and industrial applications such as solvent extraction. A quantitative understanding of these dynamic interactions at deformable interfaces is crucial for the prediction, and manipulation, of the fundamental forces in soft-matter systems.

Colloidal interaction forces between rigid particles and deformable interfaces are of considerable interest in many industrial and chemical processes, such as froth flotation and solvent extraction, and are of great importance in the food processing and personal care industries where the stability of complex emulsions is crucial. Quantitative determination of such forces is difficult due to the deformation of the interface (be it gas/liquid or liquid/liquid), making the actual measurement, and the theoretical analysis, of the data more complicated than for simple rigid–rigid interactions. Indeed the quantitative analysis of “static” interaction data, where the speed of approach of the

two interfaces is slow enough to prevent dynamic interaction, is itself nontrivial.<sup>12,13</sup>

Early experimental efforts to measure the interactions between a deformable interface and a solid concentrated on the use of air bubbles as the deformable interface. In 1994, Butt<sup>5</sup> and Ducker et al.<sup>6</sup> independently demonstrated the use of modified AFMs for the measurement of interactions between silica particles and air bubbles. Subsequently, Mulvaney et al.<sup>7</sup> demonstrated the direct measurement of the interactions between a silica particle and an *n*-decane droplet in an aqueous solution of the anionic surfactant sodium dodecyl sulfate (SDS), again using an AFM. The addition of SDS resulted in a purely repulsive interaction between the *n*-decane droplet and silica probe, since SDS adsorbs to the oil droplet but not the negatively charged silica probe particle. The use of slow scan speeds ( $< 200$  nm/s) in these experiments allowed simple modeling of the measured static interaction data, though the effect of droplet deformation was not incorporated. Snyder and et al.<sup>14</sup> also used the AFM in a qualitative measurement of the interaction between particles and deformable oil droplets, though here the particle was polymeric in nature consisting mainly of poly(styrene-*co*-acrylate).

Recently, advances have been made in the quantitative analysis of both static<sup>12,15–18</sup> and dynamic<sup>8,19</sup> interaction data recorded between a solid particle and a deformable interface using the AFM. Crucially, the theoretical interpretations presented in these articles incorporated a self-consistent account of deformations of the interface during the interaction. Nespolo and et al.<sup>17</sup> demonstrated close agreement between experimental data and theoretical interaction profiles for the static interactions between a silica particle and an *n*-decane droplet in aqueous solutions of various SDS concentrations. More recently the measurement of static<sup>9,10</sup> and dynamic<sup>11,20</sup> forces between two deformable drops using AFM has been presented, as well

\* To whom correspondence should be addressed. E-mail: gwebber@unimelb.edu.au (G.B.W.); rrd@unimelb.edu.au (R.R.D.).

<sup>†</sup> Particulate Fluids Processing Centre, The University of Melbourne.

<sup>‡</sup> Department of Chemical and Biomolecular Engineering, The University of Melbourne.

<sup>§</sup> Department of Mathematics and Statistics, The University of Melbourne.

<sup>||</sup> School of Chemistry, The University of Melbourne.

<sup>⊥</sup> Department of Mathematics, National University of Singapore.

<sup>#</sup> Institute of High Performance Computing, Singapore.

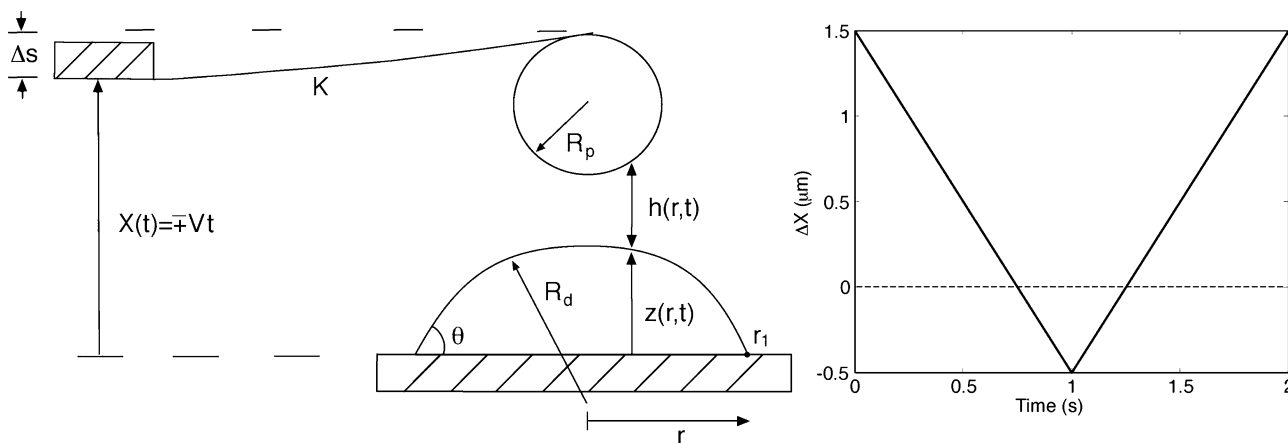


**Figure 1.** Schematic diagram of the AFM particle–drop configuration showing the cantilever deflection,  $\Delta s$ , drop height,  $z(r, t)$ , contact angle,  $\theta$ , drop contact radius,  $r_1$ , drop radius of curvature,  $R_d$ , separation,  $h(r, t)$ , particle radius,  $R_p$ , and displacement function,  $X(t)$ .

as a theoretical interpretation.<sup>11,19</sup> Herein we will extend this theory to the modeling of dynamic interaction data measured between a rigid probe particle and deformable oil droplet over a range of approach velocities.

We investigate the dynamic force between a silica particle (radius  $\sim 12 \mu\text{m}$ ) mounted on a triangular AFM cantilever and the deformable oil/water (O/W) interface of an immobilized tetradecane droplet (radius of curvature  $\sim 55 \mu\text{m}$ ). The cantilever is driven toward or retracted from the deformable O/W interface, and the resultant force is measured as a function of displacement and drive velocity. The deformable O/W interface is rendered negative by the addition of an anionic surfactant, sodium dodecyl sulfate (SDS). As a result, the colloidal force between the negatively charged particle and the deformable O/W interface is repulsive due to electrical double layer interactions. Over the range of drive velocities of up to  $50 \mu\text{m/s}$ , colloidal forces, hydrodynamic interactions due to fluid flow in the aqueous film ( $\sim 22 \text{ nm}$  thick) between the particle and the O/W interface, as well as deformations of the interface contribute to the overall dynamic force between the silica particle and tetradecane drop.

We also present a model of particle–drop interactions that takes into account surface forces, hydrodynamic interactions, and interfacial deformations in a self-consistent way and compare predicted forces with AFM measurements. The theory is also able to furnish additional information about the systems such as variations in the extent of the interfacial deformation as a function of position and time, as well as interfacial velocities of the O/W interface during the course of the interaction. In addition, position and time variations of the thickness of the aqueous film between the particle and the drop can also be inferred from the model.

## 2. Experimental Methods

An Asylum MFP-3D AFM (Asylum Research, Santa Barbara) with closed fluid cell attachment was used for the collection of all interaction data. All fluid cell components, such as o-rings and membranes, were rinsed with ethanol (AR-Grade, Sigma Aldrich, used as received) and dried under a purified nitrogen stream prior to assembly in a laminar flow cabinet. Silica colloidal particles (Potters Industries, Australia) were attached to V-shaped silicon nitride MLCT cantilevers (Veeco Probes, CA) using 2-part epoxy. The spring constant of the cantilever was determined via the thermal tune function of the MFP-3D operating software, based on the equations of Hutter and Bechhoefer.<sup>21</sup> Prior to experimentation, the glass slide bottom substrate was sputter coated with chromium ( $\sim 2 \text{ nm}$ ) and then

gold ( $\sim 10 \text{ nm}$ ) and immediately hydrophobized by immersion in decanethiol solution ( $\sim 10 \text{ mM}$  in ethanol, Sigma Aldrich, used as received) for at least 18 h.<sup>22</sup> The slide was rinsed with ethanol and dried under a stream of purified nitrogen prior to fluid cell assembly. An array of tetradecane (Sigma Aldrich, used as received) droplets were immobilized on the bottom glass slide by spraying the oil through a narrow gauge syringe-mounted needle, as described by Dagastine et al.<sup>18</sup> The oil droplets were then immersed in aqueous solution by careful injection of a  $5 \text{ mM}$  solution of anionic surfactant, sodium dodecyl sulfate (SDS, Sigma Aldrich, used as received). The radius of the silica particle,  $R_p$ , and base contact radius of the drop on the surface,  $r_1$ , were measured using optical microscopy. The undistorted radius of curvature of the oil droplet,  $R_d$ , was then calculated from the (acute) contact angle,  $\theta$ , of tetradecane on a decanethiol self-assembled monolayer using

$$r_1 = R_d \sin \theta$$

The contact angle of a sessile tetradecane drop on a gold supported decanethiol self-assembled monolayer was measured using a DataPhysics OCA 20 Tensiometer. This value of contact angle, based on a macroscopic measurement, was applied to the microscale droplets used in the AFM experiments. The variability in the contact angle due to drop hysteresis is estimated to be less than 5%, and the theory has previously been shown to be quite insensitive to changes in contact angle.<sup>23</sup> The theoretical description of the interaction forces, detailed below, assumes that the contact line of the droplet is pinned, and the contact angle is allowed to vary due to deformations in the drop. The interfacial tension was determined via the pendant drop method, using the same system.

A schematic representation of the AFM experimental configuration is shown in Figure 1. It is important to note at this stage that the piezo-electric crystal used for movement in the  $z$  axis is mounted in the tip holder of the Asylum MFP-3D AFM, and so it is the cantilever that moves during the collection of force–distance data. Additionally, the  $z$  piezo has a linear displacement voltage transformer (LVDT) sensor, so that the position of the  $z$  piezo is known throughout data collection. It is clear from Figure 1 that, because of interactions between the particle and the drop, changes in the piezo displacement,  $\Delta X$  gives rise to changes in the deflection  $\Delta s$  of the cantilever, the separation  $h(r, t)$  between the silica particle and oil droplet and the deformation of the drop. Experimentally,  $\Delta X$  is specified but the absolute value of  $X$  is not known. It is customary to assign an arbitrary origin for  $X$  and display the measured force

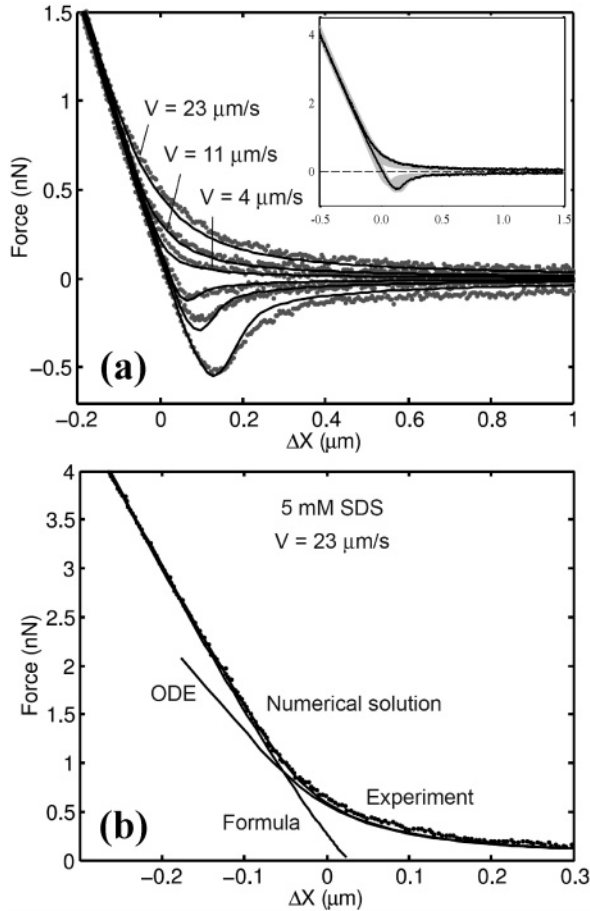


**Figure 2.** (a) Force versus displacement from AFM experiments (dots) and theory (full lines) for nominal constant drive velocities  $V = 4, 11,$  and  $23 \mu\text{m/s}$  in the range where the approach branch and the retract branch, with attractive minima, are most distinct. The force and displacement over the full measured range at  $V = 23 \mu\text{m/s}$  is shown in the inset. In all cases, the initial distance of closest approach,  $h_{\text{start}} = 1.5 \mu\text{m}$  and the maximum piezo displacement was  $\Delta X_{\text{max}} = 2 \mu\text{m}$ . See Table 1 for other experimental and theoretical parameters. The gray region of the inset shows the possible range of the theoretical data given the uncertainties in the independently measured parameters, compared to the experimental data (black line). (b) For the case  $V = 23 \mu\text{m/s}$  we compare experimental data with the approximate low force, eqs 14 and 15 labeled “ODE” and large force, eq 18 labeled “Formula” results.

$F(\Delta X)$  relative to this origin.<sup>12</sup> As such, the data displayed have been offset horizontally to allow clear comparison of features of interest. Such force vs displacement data, over a full approach and retract cycle, were recorded for a range of cantilever speeds from  $50 \text{ nm/s}$  to  $50 \mu\text{m/s}$ , though for reasons of clarity only a selection of these data are displayed. For quantitative comparison with theory (see later), we choose the value  $\Delta X = 0$  to be the position when the particle would touch the drop if neither the drop nor the cantilever deformed.

Particular care has been taken to align the particle at the apex of the drop to ensure the particle travels along the normal to the surface at the apex. This also ensures that surface deformations are expected to be axisymmetric and facilitates a simpler theoretical analysis.

The control software of the Asylum MFP-3D AFM allows the piezo to be driven at constant velocity displacements, that is, the displacement function assumes the form  $X(t) = Vt$ , where the constant velocity  $V < 0$  corresponds to approach of the particle to the drop and  $V > 0$  corresponds to retract. In fact,

**TABLE 1: Measured and Model Parameters Used in Modeling AFM Force Measurements**

parameter	measured	model
radius of silica particle, $R_p$ ( $\mu\text{m}$ )	$10 \pm 2$	12
radius of curvature of tetradecane, $R_d$ ( $\mu\text{m}$ )	$51 \pm 5$	55
cantilever spring constant, $k$ (N/m)	$0.0156 \pm 10\%$	0.017
surface potential of silica particle <sup>30</sup> (mV)	$-40 \pm 10$	-40
surface potential of tetradecane <sup>26</sup> (mV)	$-100 \pm 10$	-100
interfacial tension, $\sigma$ (mN/m)	$10 \pm 2$	8.5
contact angle, $\theta$ ( $^\circ$ )	$58 \pm 5^\circ$	$55^\circ$
SDS concentration (mM)	5	5

an examination of the LVDT data reveals that the velocity varies somewhat during the course of the approach-retract cycle. We shall return to this issue in the Discussion section. For the present, we treat the experiment as a constant velocity drive.

### 3. Model

**3.1. Governing Equations.** In the experiment, the thickness,  $h$ , of the aqueous film between the particle and the oil drop is small compared to the unperturbed radius of curvature of the drop,  $R_d$ , and of the particle,  $R_p$ , so that the familiar Stokes–Reynolds thin film drainage model applies. For a film with axial symmetry, which corresponds to experimental conditions, the governing equation for the time evolution of the film thickness,  $h(r, t)$ , is

$$\frac{\partial h}{\partial t} = \frac{1}{12\mu r} \frac{\partial}{\partial r} \left( rh^3 \frac{\partial p}{\partial r} \right) \quad (1)$$

where  $\mu$  is the shear viscosity of the aqueous film and  $p(r, t)$  is the hydrodynamic pressure in the film relative to the bulk pressure. Implicit in eq 1 is the assumption of the no-slip hydrodynamic boundary at the particle/electrolyte and O/W interface. The presence of surfactants at the O/W interface justifies the use of the no-slip hydrodynamic boundary condition<sup>24–26</sup> as we have no indications that surfactant transport phenomena play a role during interaction. Although the possibility of slip at either interface cannot be discounted a priori, the no-slip model has the least number of unknown parameters. With the no-slip condition, hydrodynamic flow inside the oil drop need not be considered. Furthermore, there is evidence that theoretical predictions with the no-slip boundary condition offer the best agreement between experiment and theory involving deformable surface studies on other experiments based on the AFM<sup>11,19</sup> and on the surface force apparatus.<sup>27–29</sup>

The axisymmetric deformations of the drop as it interacts with a rigid surface with local radius of curvature,  $R_p$ , consistent with the thin film approximation, is governed by the modified Young–Laplace equation<sup>11,19</sup>

$$\frac{\sigma}{r} \frac{\partial}{\partial r} \left( r \frac{\partial h}{\partial r} \right) = \frac{2\sigma}{R_{\text{eff}}} - (p + \Pi) \quad (2)$$

where  $\Pi(h(r, t))$  is the disjoining pressure in the film due to surface forces such as electrical double layer interactions or van der Waals forces,  $\sigma$  is the interfacial tension of the drop populated with surfactants,  $R_{\text{eff}}^{-1} = (R^{-1} + R_p^{-1})$  and  $(2\sigma/R)$  is the Laplace pressure of the drop.

The instantaneous force,  $F(t)$  exerted on the drop has contributions from hydrodynamic and disjoining pressures

$$F(t) \equiv 2\pi\sigma G(t) = 2\pi \int_0^\infty (p(r,t) + \Pi(h(r,t)))r dr \quad (3)$$

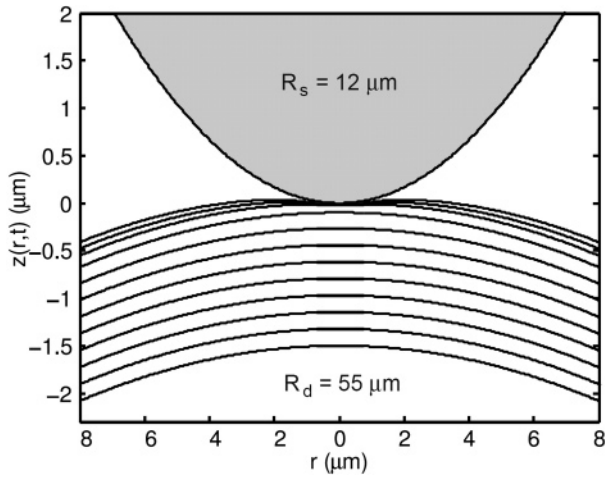


**Figure 3.** Variations of the drop profile during the course of interaction with the particle. The radial extent of the interaction zone is less than  $2 \mu\text{m}$  compared to the particle radius ( $12 \mu\text{m}$ ) and the drop radius ( $55 \mu\text{m}$ ). Over the interaction zone, the parabolic approximation to the particle shape is adequate.

As we shall see, the quantity  $G(t)$ , with dimension of length, enters naturally in characterizing the deformation of the drop during interaction.

Equations 1 and 2 are to be solved numerically in a suitable radial domain  $0 < r < r_{\text{max}}$ , where  $r_{\text{max}}$  is chosen to be outside the film where the film thickness is sufficiently large so that effects due to the disjoining pressure are negligible, but  $r_{\text{max}}$  is still small compared to the drop radius  $R_d$ . In practice, computational results are independent of the exact value of  $r_{\text{max}}$ .

The initial film thickness when the particle and the drop are far apart has the form

$$h(r, t_{\text{start}}) = h_{\text{start}} + \frac{r^2}{2R_0} \quad (4)$$

with the assumption that the drop is initially undeformed:  $R_0^{-1} = (R_d^{-1} + R_p^{-1})$ . Symmetry considerations require  $\partial h/\partial r = 0$  and  $\partial p/\partial r = 0$  at  $r = 0$ . At the outer boundary  $r \sim r_{\text{max}}$ , the expected asymptotic form of the pressure  $p \sim r^{-4}$  for large  $r$  is implemented as the condition

$$\frac{\partial p}{\partial r} + \frac{4}{r}p = 0 \text{ at } r = r_{\text{max}} \quad (5)$$

The integral for the force can be evaluated as

$$F(t) \cong 2\pi \int_0^{r_{\text{max}}} (p(r,t) + \Pi(h(r,t)))r \, dr + 2\pi \int_{r_{\text{max}}}^{\infty} p(r,t)r \, dr \quad (6)$$

since in the second integral  $r_{\text{max}}$  has been chosen so that the contribution from the disjoining pressure is negligible and the asymptotic form of the pressure  $p$  is used to evaluate the integral directly.

A further boundary condition can be derived from the fact that the drops interact and deform under a constant volume constraint during the approach and retraction phases of the experiment.

It has been shown that when a sessile drop with an equilibrium contact angle  $\theta$  (see Figure 1) and unperturbed drop height  $z_0$  is subjected to an applied force that is localized around

the apex, the perturbed drop height,  $z^{\text{outer}}(r)$ , outside the zone in which the force acts has the following asymptotic form as the drop deforms under constant volume:<sup>12</sup>

$$z^{\text{outer}}(r) \cong z_0 - \frac{r^2}{2R} + G \left[ \log\left(\frac{r}{2R_d}\right) + B(\theta) \right] \quad (7)$$

where  $z_0 = z(r = 0, t = 0)$  is the unperturbed height of the drop at the apex. The constant  $B(\theta)$  depends whether during deformation, the three phase contact line (TPL) remains pinned or is free to slip on the substrate to maintain the equilibrium contact angle

$$B(\theta) = \begin{cases} 1 + \frac{1}{2} \log\left(\frac{1 + \cos \theta}{1 - \cos \theta}\right), & \text{pinned TPL} \\ 1 + \frac{1}{2} \log\left(\frac{1 + \cos \theta}{1 - \cos \theta}\right) - \frac{1}{2 + \cos \theta}, & \text{slip TPL} \end{cases} \quad (8)$$

Equation 7 for the drop profile, which reflects the constant volume constraint on the deforming sessile drop, is an expansion correct to first order in  $(G/R_d)$ . This result together with the geometric condition (see Figure 1)

$$X(t) = h(r,t) + z(r,t) - \frac{r^2}{2R_p} - \Delta s + \text{constant} \quad (9)$$

gives the required boundary condition at  $r_{\text{max}}$  by a differentiation with respect to  $t$  to eliminate the constants

$$\frac{dX}{dt} = \frac{\partial h}{\partial t} + \left[ \log\left(\frac{r_{\text{max}}}{2R_d}\right) + B(\theta) - \frac{2\pi\sigma}{K} \right] \frac{dG}{dt} \text{ at } r = r_{\text{max}} \quad (10)$$

Equation 10 is the appropriate constant drop volume boundary condition for experiments in which the variation of the displacement function  $X(t)$  with time  $t$  is specified. The effect of driving the particle and drop together enters as the boundary condition via eq 10 in determining the film drainage and surface deformations described by the Reynolds and Young–Laplace equations, eqs 1 and 2. The term proportional to  $(dG/dt)$ , see eq 3, accounts for effects due to deformations of the drop outside the interaction zone under a constant volume constraint, as well as cantilever deflections. Also it is clear from eq 10 that the instantaneous local velocity of the drop surface  $(\partial h/\partial t)$  will not be constant along the surface and even at  $r_{\text{max}}$  the local velocity will be different from the drive velocity  $dX(t)/dt$ . We will illustrate this point in the results section.

The governing eqs 1–10 can be solved by the method of lines that involves converting the system of partial differential equations into a set of about 200 coupled differential algebraic equations. Typically, the domain size of our numerical solution satisfies  $r_{\text{max}}/R_d, r_{\text{max}}/R_p < 0.1$  and deformations and forces are ascertained to be independent of the choice of  $r_{\text{max}}$ .<sup>19</sup> The solution of eq 1–10 requires physical input parameters, such as interfacial tension, surface potentials, viscosities and drive velocities etc., that can be measured independently. There are no free parameters in the model apart from the initial position of the piezo drive that cannot be determined. However, in any set of experimental runs, the initial position does not vary significantly. The major uncertainties in this model are dictated by the measurement tolerance of the physical parameters of the system.

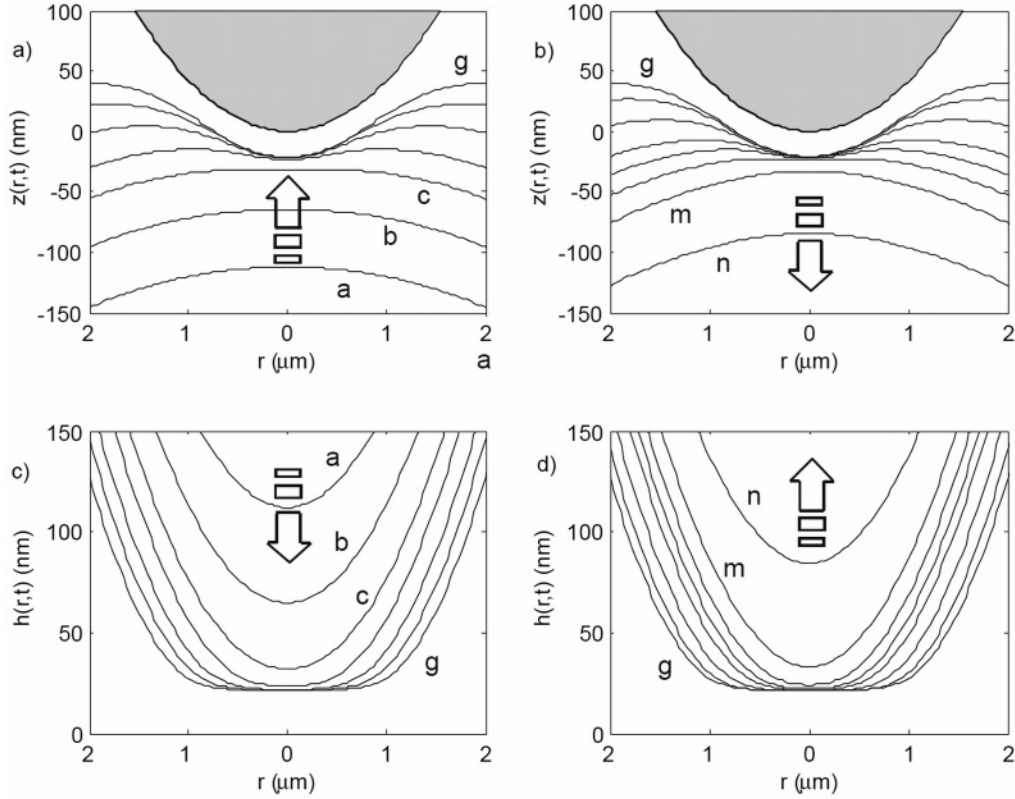


**Figure 4.** Evolution of the calculated drop profile  $z(r, t)$  during (a) the approach phase (*a..g*) and (b) the retract phase (*g..n*). The corresponding thicknesses of the aqueous film between the drop and the particle during (c) approach and (d) retract are also shown. Labels *a...n* correspond to various points on the force–displacement curve in Figure 5.

Before we compare full numerical solutions of the above governing equations of the model with experimental results, we first give two limiting solutions that are valid for small forces or for large forces that proved to be rather accurate in accounting the approach branch of dynamical particle-drop interaction. For both of these solutions it is convenient to define the modified displacement function  $\Delta Y(t)$ , given by

$$\Delta Y(t) = \Delta X(t) + \Delta s(t) \quad (11)$$

$\Delta Y$  would represent the absolute separation between the particle and the drop (at  $r = 0$ ) if the drop did not deform, but with allowance for the deflection of the cantilever.

**3.2. Small Force Limit.** In a recent paper,<sup>29</sup> we developed a simplified solution for the governing eqs 1–10 which is valid when the interaction is weak and only included hydrodynamic interactions and surface deformations, while omitting effects due to disjoining pressure. These assumptions are valid when the particle and the drop are far apart and disjoining pressure interactions are small compared to hydrodynamic interactions. This solution is cast in terms of scaled variables using the capillary number  $Ca = (\mu V/\sigma)$ .<sup>25</sup>

$$\begin{aligned} \{G, \Delta X, h\} &\sim (Ca^{1/2} R_{\text{eff}}) \\ r &\sim (Ca^{1/4} R_{\text{eff}}) \\ \{p, \Pi\} &\sim (\sigma/R_{\text{eff}}) \\ t &\sim (Ca^{-1/2} R_{\text{eff}} t/\sigma) \end{aligned} \quad (12)$$

In these scaled variables (indicated by the \*), we seek a solution of the form

$$h^*(r^*, t^*) = a^*(t^*) + \frac{1}{2} r^{*2} \quad (13)$$

where  $a^*(t^*)$  is the solution of the ordinary differential equation

$$\frac{3}{a^*(t^*)} \frac{da^*(t^*)}{dt^*} \left[ \left( B(\theta) + \log \left( \frac{Ca^{1/4} R_p}{2(R_d + R_p)} \right) \right) + \frac{1}{2} \log(2a^*(t^*)) \right] - a^*(t^*) = -\Delta Y^*(t^*) \quad (14)$$

This differential equation for  $a^*(t^*)$  is obtained by eliminating  $p$  from between eqs 1 and 2 and then substituting eq 13 into the result to obtain a result that, for large  $r$ , must match to the outer solution given by eq 7. By setting  $f^*(t^*) = \log(a^*(t^*))$ , the numerical solution of eq 14 is straightforward to determine and the force, eq 6, can be expressed in terms of this dimensionless function  $f^*(t^*)$ , which is a function of the dimensionless time according to the scaling in eq 12

$$F = -6\pi\sigma Ca^{1/2} \frac{R_d R_p}{R_d + R_p} \frac{df^*}{dt^*} \quad (15)$$

The range of applicability of this approximation will be demonstrated in the results section by comparison with experiments.

**3.3. Large Force Limit.** A simple expression for the force valid in the large repulsion limit, in the context of surface force measurement, of repulsive dynamical interactions has been developed.<sup>29</sup> When the particle is pushed into the drop and the dynamic pressure ( $p + \Pi$ ) remains repulsive, an aqueous film of thickness  $h_f$  will form between the particle and the drop. This dynamic film thickness is given by the condition  $(p + \Pi) = (2\sigma/R_{\text{eff}})$  at  $h_{\text{eff}}$ , and from eq 2, this implies that the curvature of this film is zero. From a first integral of eq 2, we can obtain

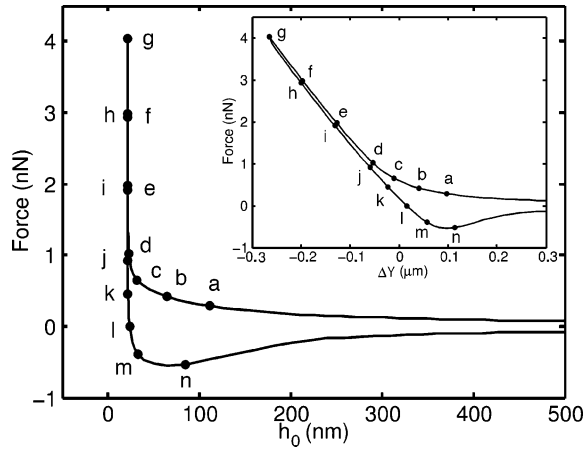


**Figure 5.** Variation of the force with the central separation  $h_0 = h(0, t)$  along the approach and the retract branch for  $V = 23 \mu\text{m/s}$ . Points (a...n) indicate corresponding values on the force-displacement graph (inset); the corresponding surface deformations and film thicknesses are shown in Figure 4.

an estimate of the radial extent,  $a \approx (G R_{\text{eff}})^{1/2}$  of the dynamical film as the radial position at which  $(\partial h/\partial r)$  begins to become positive.

The large  $r$  limit of the inner solution of the drop height has the form<sup>19</sup>

$$z^{\text{inner}}(r, t) \cong z(0, t) - \frac{r^2}{2R} + G \log r - \frac{1}{\sigma} \int_0^\infty (p + \Pi) r' \log r' dr' \quad (16)$$

where  $z(0, t)$  is the perturbed height of the drop at  $r = 0$ . When the dynamic film of thickness  $h_f$  has formed, the integral in eq 16 can be evaluated by using the approximation  $(p + \Pi) = (2\sigma/R_{\text{eff}})$  for  $0 < r < a$  but vanishes for  $r > a$ . By requiring the outer, eq 7, and inner, eq 16, solutions to match, we have an expression for the deformation of the drop apex given by

$$z_o - z(0, t) \cong -\frac{F}{4\pi\sigma} \left[ \log\left(\frac{FR_o}{8\pi\sigma R_d^2}\right) + 2B(\theta) - 1 \right] \quad (17)$$

where to leading order in  $(G/R_d)$  we have made the approximation  $R_{\text{eff}}^{-1} \equiv R^{-1} + R_s^{-1} \approx R_d^{-1} + R_s^{-1} \equiv R_o^{-1}$ .

Recalling that  $\Delta Y$  is defined to be the separation that would exist between particle and drop if the latter did not deform, and remaining cognizant of that fact that the particle and the drop cannot approach closer than the dynamic film thickness  $h_f$ , we have the desired approximate relationship between the displacement and the repulsive force during the approach branch of the dynamical interaction

$$\Delta Y \cong h_f - [z_o - z(0, t)] \cong h_f + \frac{F}{4\pi\sigma} \left[ \log\left(\frac{FR_o}{8\pi\sigma R_d^2}\right) + 2B(\theta) - 1 \right] \quad (18)$$

With the appropriate expression for  $B(\theta)$  from eq 8, the result in eq 18 is valid for both the pinned or free-to-slip three phase contact line condition and for acute or obtuse contact angles,  $\theta$ . In the next section, we will see how well eq 18 compares with experimental data in the large repulsive force regime.

Apart from being a simple approximate result for the force-displacement relationship in the repulsive branch of the force curve, an important consequence of eq 18 is the nonlinear nature

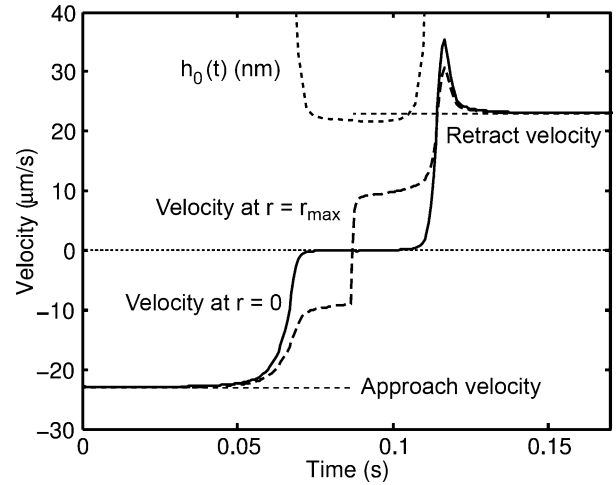


**Figure 6.** Variation of the interfacial velocity of the drop  $(\partial h/\partial t)$  at  $r = 0$  (solid line) and  $r = r_{\text{max}}$  (dashed line), and the central thickness of the film  $h_0(t) = h(0, t)$  (dotted line) at a drive velocity of  $\pm 23 \mu\text{m/s}$ . The unit of vertical axis is in  $\mu\text{m/s}$  for the velocity  $(\partial h/\partial t)$  curves and in nm for the central film thickness curve  $h_0(t)$ .

of the force-displacement relationship over the typical range force magnitudes. This has important implications in determining the constant compliance region of AFM experiments. Earlier work on the interpretation of direct force measurements involving deformable drops and bubbles assume they behave as Hookean springs, that is, their deformation is assumed to be linear with applied force.<sup>5,6</sup>

#### 4. Results and Discussion

In Figure 2, we see that, for drive velocities between 4 to 23  $\mu\text{m/s}$ , the measured force as a function of piezo displacement exhibit a velocity dependent hysteresis between the approach and retract branches of the force curve. Along the approach branch, the force is always repulsive with stronger repulsion at higher velocities. Along the retract branch, the force shows a characteristic attractive minimum whose depth increases with increasing velocity (Figure 2a). At high forces, between 1 and 4 nN (Figure 2a, inset), the force curves are independent of velocity in the range considered.

Using measured data summarized in Table 1 as input, the full numerical solution of the model given in eqs 1–10, together with the Poisson–Boltzmann theory to describe the electrical double layer interaction between the silica particle and the SDS coated oil drop, gave excellent agreement with experimental data. This is strong evidence that the model has captured the essential physics of this problem and therefore one can confidently interrogate the model to extract physical insight about the dynamical interaction between a solid particle and a deformable drop.

In Figure 2b, we show the agreement between the two simplified small and large force limit forms of the theory for the approach branch at a drive velocity of 23  $\mu\text{m/s}$ . The low force limit described in eqs 14 and 15 agrees with the force data at low to moderate forces where hydrodynamic forces dominate the force and deformation between the particle and the drop. At higher forces, the low limit force form deviates as the effects from disjoining pressure become more significant. The high force limit model given in equation eq 18 shows good agreement over a large force range. It is important to note that the two surfaces are not in contact and the droplet continues to deform even though the force branch in this region appears pseudolinear and similar to a constant compliance region in a

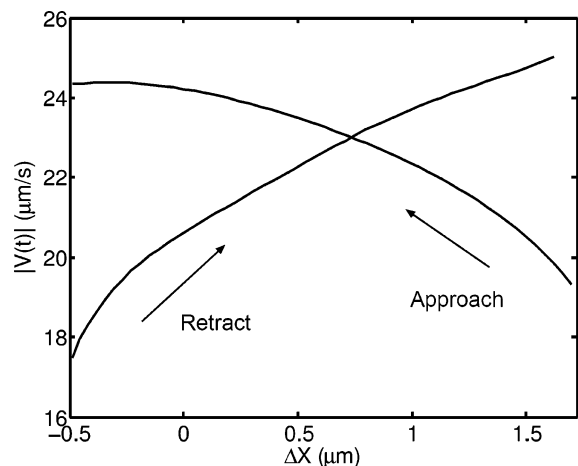


**Figure 7.** LVDT data of the variations of the actual speed of the drive when the Asylum MFP-3D controlling software has been set to drive at a nominal speed of  $20 \mu\text{m/s}$ .

force curve between two rigid surfaces. These limiting forms offer a great deal of utility in analysis of these types of data with fast and straightforward calculations.

In Figure 3, we show the fluid interface predicted by the model during the course of the interaction between the particle and the drop. It is important to note that the radial dimension of the interaction region between the particle (of radius  $12 \mu\text{m}$ ) and the drop is less than  $2 \mu\text{m}$ , which constitute only small fraction of the drop radius ( $55 \mu\text{m}$ ). Thus the deformation of the O/W in is very small on the scale of the drop size.

In Figure 4, we show details of the oil drop profiles  $z(r, t)$  in the interaction zone as predicted by the model during the approach (Figure 4a) and retract phases (Figure 4b). From Figure 4c,d, we see that the thickness,  $h(r, t)$  of the aqueous film between the drop and the particle is no less than  $h_{\text{eq}} \sim 22 \text{ nm}$ , which is given by the condition  $\Pi(h_{\text{eq}}) = (2\sigma/R_{\text{eff}})$  where  $\Pi(h)$  in the present system is the disjoining pressure due to electrical double layer repulsion between the drop and the particle. This leads to an aqueous film  $\geq 22 \text{ nm}$  thick with a radial dimension of  $1\text{--}2 \mu\text{m}$ , yet unlike the case of the interaction between a mercury drop and a mica surface,<sup>27</sup> the film thickness,  $h(r, t)$  for the present particle-drop system shows no signs of dimple formation within the range of present experimental parameters.

In Figure 5, we show the variation of the force with the central separation  $h_0 = h(0, t)$  along the approach and the retract branch for  $V = 23 \mu\text{m/s}$ . The points marked as (a..n) correspond to the values on the force–displacement graph in the inset and also to the corresponding surface deformations profiles and film thicknesses that are shown in Figure 4. The force vs central separation plot is unlike a traditional force vs separation plot for static forces because this is in fact a dynamic force trajectory over the approach and retract path of the particle. Figure 5 is effectively a plot of force and central separation that is parametric in time where each point corresponds to both a force and a direction. If for example one compares the curves marked *b* and *n* in Figure 4, it is clear that the deformation profiles are very similar, but the forces are not simply equal in magnitude but opposite in sign due to the time dependent history of the motion from points *b* to *n*. These types of distinctions become important when dynamic forces are compared to static forces.

Variations of the velocity,  $(\partial h/\partial t)$  of the drop interface at  $r = 0$  and at  $r = r_{\text{max}}$  during approach and retract are shown in Figure 6. At any time, velocities at other points on the interface in  $0 < r < r_{\text{max}}$  lie between these two curves. It is interesting to observe that at the end of the retraction phase, the interfacial

velocity at the axis of symmetry  $r = 0$ , rises briefly to around  $35 \mu\text{m/s}$ , and overshoots the drive velocity of  $23 \mu\text{m/s}$  as the particle separates rapidly from the O/W interface, as indicated by the rapid increase of the distance of closest approach  $h_0(t) = h(0, t)$ .

## 5. Conclusion

In this study we have demonstrated successfully the use of a colloid particle probe mounted on the cantilever of an atomic force microscope to measure the time dependent dynamic force between a silica particle and deformable tetradecane/electrolyte interface stabilized by added SDS. Within the measured tolerance of system parameters, the measured force-displacement data are in pleasing agreement with a model that accounts for colloidal forces, hydrodynamic interactions and surface deformations in a self-consistent manner. This model also provides insight about the phenomena inside the interaction zone such as drop surface deformation, film thickness, interfacial velocities and particle-drop separation that cannot at present be measured. This opens up exciting opportunities to use the same methodology to explore more complex deformable surfaces and probe dynamic events such as surface elasticity, surface rheology and effects due to material transfer across interfaces. The possibility to functionalize the particle probe or to replace it with another deformable body is another avenue of exploration.

This work also augments earlier AFM measurements of forces between two deformable drops.<sup>11,20</sup> The use of a solid particle probe instead of a drop on the cantilever removes any possible ambiguity as to the location load point on the cantilever. The demonstrated success of both types of experiments confirms the utility and methodology of force measurement experiments involving deformable bodies.

One final observation regarding the behavior of the current version of the Asylum MFP-3D AFM (Asylum Research, Santa Barbara) may be in order. An examination of the LVDT data show that, although the piezo can be driven at a nominally constant drive speed, it is common to operate the Asylum AFM where the controlling software actually runs the cantilever at a variable speed (Figure 7).<sup>31</sup> We have ascertained that this variation is not significant in the present study because it is masked by variations in other system parameters. However, this idiosyncratic behavior of the AFM may be important in other applications.

**Acknowledgment.** This work has been supported in part by the Particulate Fluids Processing Centre, a Special Research Centre of the Australian Research Council. R.M. is supported by a University of Melbourne International Research Scholarship. D.C. is supported by a Visiting Professorship at the National University of Singapore and an adjunct appointment at the Institute of High Performance Computing.

## References and Notes

- (1) Ducker, W. A.; Senden, T. J.; Pashley, R. M. *Nature* **1991**, *353*, 239–41.
- (2) Claesson, P. M.; Ederth, T.; Bergeron, V.; Rutland, M. W. *Adv. Colloid Interface Sci.* **1996**, *67*, 119–184.
- (3) Craig, V. S. J. *Colloids Surf. A* **1997**, *129*, *130*, 75–94.
- (4) Hartley, P. G. *Colloid-Polym. Interact.* **1999**, 253–286.
- (5) Butt, H.-J. *J. Colloid Interface Sci.* **1994**, *166*, 109–17.
- (6) Ducker, W. A.; Xu, Z.; Israelachvili, J. N. *Langmuir* **1994**, *10*, 3279–89.
- (7) Mulvaney, P.; Perera, J. M.; Biggs, S.; Grieser, F.; Stevens, G. W. *J. Colloid Interface Sci.* **1996**, *183*, 614–616.
- (8) Aston, D. E.; Berg, J. C. *Ind. Eng. Chem. Res.* **2002**, *41*, 389–396.

- (9) Dagastine, R. R.; Stevens, G. W.; Chan, D. Y. C.; Grieser, F. *J. Colloid Interface Sci.* **2004**, *273*, 339–342.
- (10) Dagastine, R. R.; Chau, T. T.; Chan, D. Y. C.; Stevens, G. W.; Grieser, F. *Faraday Discuss.* **2005**, *129*, 111–124.
- (11) Dagastine, R. R.; Manica, R.; Carnie, S. L.; Chan, D. Y. C.; Stevens, G. W.; Grieser, F. *Science* **2006**, *313*, 210–213.
- (12) Chan, D. Y. C.; Dagastine, R. R.; White, L. R. *J. Colloid Interface Sci.* **2001**, *236*, 141–154.
- (13) Bhatt, D.; Newman, J.; Radke, C. J. *Langmuir* **2001**, *17*, 116–130.
- (14) Snyder, B. A.; Aston, D. E.; Berg, J. C. *Langmuir* **1997**, *13*, 590–593.
- (15) Aston, D. E.; Berg, J. C. *J. Colloid Interface Sci.* **2001**, *235*, 162–169.
- (16) Dagastine, R. R.; White, L. R. *J. Colloid Interface Sci.* **2002**, *247*, 310–320.
- (17) Nespolo, S. A.; Chan, D. Y. C.; Grieser, F.; Hartley, P. G.; Stevens, G. W. *Langmuir* **2003**, *19*, 2124–2133.
- (18) Dagastine, R. R.; Prieve, D. C.; White, L. R. *J. Colloid Interface Sci.* **2004**, *269*, 84–96.
- (19) Carnie, S. L.; Chan, D. Y. C.; Lewis, C.; Manica, R.; Dagastine, R. R. *Langmuir* **2005**, *21*, 2912–2922.
- (20) Dagastine, R. R.; Chau, T. T.; Chan, D. Y. C.; Stevens, G. W.; Grieser, F. *World Congress of Chemical Engineering*, 7th, Glasgow, United Kingdom July 10–14, 2005; 86500/1–86500/9.
- (21) Hutter, J. L.; Bechhoefer, J. *Rev. Sci. Instrum.* **1993**, *64*, 1868–73.
- (22) Wall, J. F.; Grieser, F.; Zukoski, h. F. *J. Chem. Soc. Faraday Trans.* **1997**, *93*, 4017–4020.
- (23) Carnie, S. L.; Chan, D. Y. C.; Manica, R. *ANZIAM J.* **2005**, *46*, C805–C819.
- (24) Baygents, J. C.; Saville, D. A. *J. Chem. Soc. Faraday Trans.* **1991**, *87*, 1883–98.
- (25) Klaseboer, E.; Chevaillier, J. P.; Gourdon, C.; Masbernat, O. *J. Colloid Interface Sci.* **2000**, *229*, 274–285.
- (26) Nespolo, S. A.; Bevan, M. A.; Chan, D. Y. C.; Grieser, F.; Stevens, G. W. *Langmuir* **2001**, *17*, 7210–7218.
- (27) Manica, R.; Connor, J. N.; Carnie, S. L.; Horn, R. G.; Chan, D. Y. C. *Langmuir* **2007**, *23*, 626–637.
- (28) Manica, R.; Connor, J. N.; Clasohm, L. Y.; Carnie, S. L.; Horn, R. G.; Chan, D. Y. C. *Langmuir* **2007**, in press.
- (29) Manica, R.; Connor, J. N.; Dagastine, R. R.; Carnie, S. L.; Horn, R. G.; Chan, D. Y. C. *Phys. Fluids* **2007**, in press.
- (30) Hartley, P. G.; Larson, I.; Scales, P. J. *Langmuir* **1997**, *13*, 2207–2214.
- (31) Semin, B.; Guriyanova, S.; Bonaccorso, E. *Rev. Sci. Instrum.* **2006**, *77*, 116107–116111.